Experimental and numerical investigation of 3-D corner separation in a channel flow with adverse pressure gradient

Joachim Klinner, Michael Schroll, Christian Morsbach, Felix Möller, and Christian Willert[1]

DLR Institute of Propulsion Technology, Deutsches Zentrum für Luft- und Raumfahrt, 51170 Köln, Germany,
joachim.klinner@dlr.de,
WWW home page: http://www.dlr.de/at/

Abstract. Measurements of a plane one-sided diffuser with a variable expansion ratio are compared with RANS simulations at a Reynolds number of 51,000. Two-component PIV provides boundary conditions and a global validation of mean velocities. Profile PIV is applied to evaluate the wall shear stress and to measure turbulence statistics. Typical measurement uncertainties found in the buffer layer and in the separation region are below 1% for the mean and below 6% for the Reynolds stresses. Consistency of turbulence statistics is demonstrated by comparison with DNS. A first comparison with RANS simulations reveal significant differences between the eddy viscosity model and both Reynolds stress models, which predict qualitatively different developments of the vortex system over the corner separation.

Keywords: particle image velocimetry, PIV, skin friction measurements, RANS, Reynolds stress model, diffuser, validation experiment

1 Introduction

Scale-resolving simulation approaches promise the benefit of higher predictive accuracy because they require less complex physical models. However, their application for high Reynolds number flows in an industrial environment on a day-to-day basis is still decades away due to limited computational resources [7]. Hence, Reynolds-averaged Navier-Stokes (RANS) models will remain in high demand. Modern designs require increasingly accurate prediction not only of the flow around aerofoils but also of the complex secondary flow patterns in turbomachines such as vortex systems and three-dimensional flow separation. It is these kinds of flows where RANS models based on the Boussinesq assumptions reach their limits and Reynolds stress turbulence models offer a promising framework. To assess and further improve these models, high quality reference data with well documented boundary conditions and isolated physical effects are crucial. Hence, a generic experiment was designed in the framework of DLR project *VicToria*

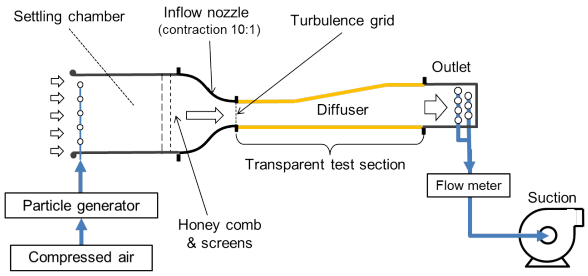

Fig. 1. Schematic diagram of the APG laboratory wind tunnel.

to investigate 3-D separated flow, which occur at end wall/blade junctions. In the following, we will introduce the experiment, describe the measurement techniques and offer a first comparison with RANS simulations.

2 Experimental procedure

2.1 Wind tunnel facility and operation conditions

Experiments are conducted in a small-scale wind tunnel with a test section consisting of a plane diffuser with turbulent inflow. The wind tunnel (see Fig 1) is operated in suction mode and has a 1000 mm long test section with a square inlet cross-section of internal width of $h^2 = 76 \times 76\,\mathrm{mm}^2$. The modular design of the wind tunnel allows experiments with different expansion ratios (ER) by setting different inclinations of the top wall in the diverging section. Two configurations have been considered, namely ER = 2.0 and ER = 2.3. Therefore, after an inlet length of $4\,h$, the cross-sectional area is expanded by a factor of 2.0 or 2.3 over a running length of $6\,h$ by opening a single side only.

Flow conditioning upstream of the test section is provided by a settling chamber containing screens and straightening tubes followed by a rectangular nozzle of 10:1 area-contraction. Reproducible turbulent flow conditions are provided by a turbulence grid that is placed immediately upstream of the test section. Along the center line and immediately upstream of the diverging section, turbulent fluctuations decay to a level of Tu = 0.023. At reference conditions (T_r=293.15 K, p_r=1013.25 hPa, $\dot{m}$=70 g/s) the bulk inlet velocity is $U_0 = 10\,\mathrm{m/s}$ and the channel Reynolds number based on h is $\mathrm{Re}_0 = 51,000$.

The wall pressure distributions are measured through multiple pressure ports placed 4 mm off the center plane of the top and the bottom wall of the test section to avoid shading of the PIV light sheet. All pressures are referenced to the lowest wall pressure (p_0), measured near the onset of the diverging section and are obtained as follows:

$$c_\mathrm{p} = \frac{2\,(p - p_0)}{\varrho(U_0 \frac{p_\mathrm{r}}{T_\mathrm{r}} \frac{T_\mathrm{T}}{p_\mathrm{T}})^2}\,, \tag{1}$$

where stagnation pressure p_T and temperature T_T are used to scale different inlet velocities to consistent reference conditions (T_r, p_r) while the mass flow is kept

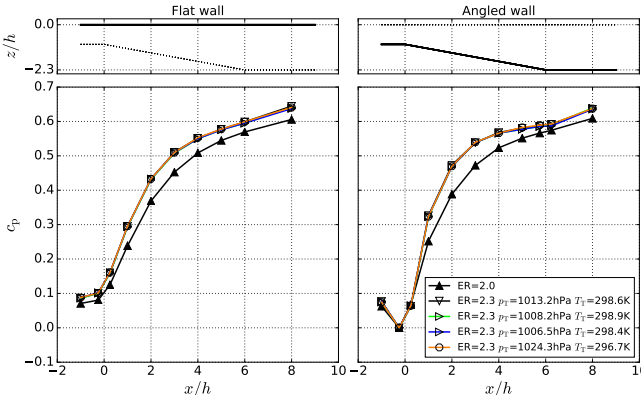

Fig. 2. Wall pressure distribution with diffuser geometry on top; Several measurements are added to demonstrate reproducibility at different days with different air densities.

constant during tunnel operation. Fig. 2 shows the wall pressure distributions for both tunnel geometries and demonstrates reproducibility at different measuring days with varying air densities.

The origin of coordinate system is located on the centerline of the flat wall coincident with the start of the ramp. The X-axis is aligned with the streamwise direction, the Y-axis defines the spanwise direction while the Z-axis coincides with the expansion direction of the channel.

2.2 Particle image velocimetry

In order to provide the mean flow distribution upstream and inside the diffuser, planar two component (2D-2C) PIV was applied successively at several stations that cover large parts of the diffuser cross-section in three spanwise planes. Furthermore, to provide boundary conditions, PIV measurements are acquired for nine spanwise planes in the square inlet cross-section at two upstream camera stations. Details on the PIV setup are provided in [4].

Detailed measurements of the evolution of the APG boundary layer and corresponding skin friction distribution are obtained by means of high resolution 1D-2C PIV profile measurements [8] at 63 stations per configuration. With the intention of providing validation data for RANS, large numbers of temporally uncorrelated (i.e. statistically independent) PIV samples ensured converged turbulence statistics even for higher moments such as variances and covariance. For the velocity profile measurements, small wall-normal measurement regions of $35 \times 2.7\,\mathrm{mm}^2$ are imaged using a double-frame camera (ILA.SCMOS.PIV) and a Nikkor Micro f=105 mm lens at a magnification of 13.7 μm/pixel and a image sizes of 2560×200 pixels . Tracer illumination in a small, 2.5 mm wide and $\approx 300\,\mu$m thin light sheet is provided by a diode pumped solid state laser (nanio Air, Innolas Photonics) that generates laser pulse bursts of variable pulse separation at repetition rates of 200 Hz. Using the same seeding system as described in [4], a sufficiently high particle tracer density could be achieved to allow image evaluation with an interrogation window size of 64×6 pixels $(0.86 \times 0.081\,\mathrm{mm}^2)$

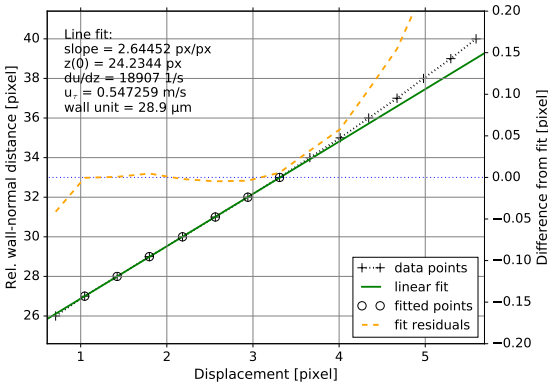

Fig. 3. Evaluation of the mean wall gradient at single pixel resolution (1 pixel $= 13.7\,\mu$m) on the inlet at $x = -1h$, $y = 0$, $z = -1h$: The gradient is obtained by a linear fit based on points marked with a circle.

and a spatial sampling of 24×2 pixels ($0.324 \times 0.027\,\mathrm{mm}^2$). Validation rates near 100% were consistently achieved throughout the profile. All PIV images are processed using PIVview 3.8.0 (PIVTEC GmbH) and the in-house PyPIVview library. For wall gradient estimation, single pixel resolution is achieved by cross-correlation of single, wall parallel image lines. Fig. 3 shows exemplarily the wall distance versus the mean tracer displacements, which were obtained by averaging the cross-correlation results in the lowest image rows near the wall. The measuring position lies $1h$ upstream from the diverging section, where relatively large wall gradients occur compared to further downstream positions. By linear regression, a constant slope is confirmed within residuals of ± 0.05 pixel at wall distances up to nine pixels or $123\,\mu$m or four wall units. The wall gradient $\mathrm{d}u/\mathrm{d}z$ is determined from the slope divided by the laser pulse separation time Δt. From the wall gradient, the skin friction coefficient c_f is obtained by normalization with the inlet dynamic pressure using the following equations

$$\begin{aligned} \tau_\mathrm{w} &= \mu \left.\frac{\partial u}{\partial z}\right|_{z=0} \\ c_\mathrm{f} &= \frac{2\,\tau_\mathrm{w}}{\varrho (U_0 \frac{p_\mathrm{r}}{T_\mathrm{r}} \frac{T_\mathrm{T}}{p_\mathrm{T}})^2}. \end{aligned} \tag{2}$$

In this context, it should be pointed out that, compared to other skin friction measurement techniques, this technique provides measures of the local wall shear stress, both unsteady and time-averaged and is essentially *calibration-free* as only the laser pulse separation needs to be known to estimate the velocity gradient at the wall from which the wall shear stress τ_w is determined using the above expression.

2.3 Accuracy estimation for velocity and turbulence statistics

The uncertainty of statistical quantities as mean, variances and covariances of velocity is obtained by bootstrapping [1] which is a resampling technique that does not require a-priory knowledge of the shape of the error distribution. To

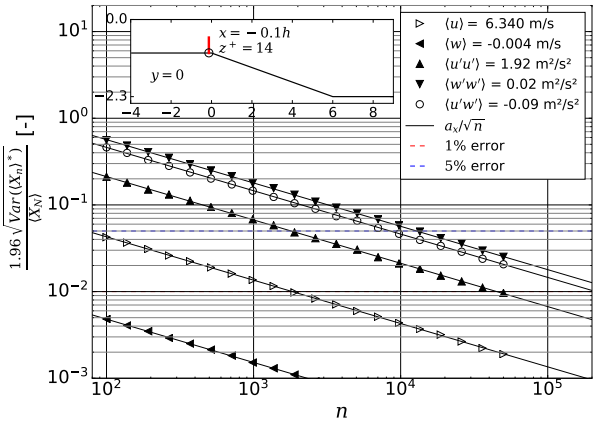

Fig. 4. Convergence of measurement uncertainty for an interrogation window near the ramp onset at the channel's symmetry plane for ER 2.3; window coordinates are given in the subplot and are marked by a circle.

estimate the statistical error from a set of PIV samples a random subset is constructed with replacement from which the target quantity $\langle X\rangle$ (i.e. mean, variance or covariance) is computed. The random choice of subsets is repeated several times to obtain a distribution of bootstrap sample quantities $\langle X\rangle^*$. For a choice of 5000 subsets the 95% confidence interval equals $2 \cdot 1.96 \cdot \mathrm{Var}(\langle X\rangle^*)^{0.5}$ which confirms a normal error distribution for each measured quantity.

Fig. 4 shows the convergence of the half confidence interval for an interrogation window slightly upstream of the ramp onset at $z^+ = 14$, where large axial velocity fluctuations occur. For velocity components U and W the relative measurement error (ordinate in Fig. 4) is obtained by normalization to the mean velocity magnitude at each measurement point. The relative error of Reynolds stress components is obtained through normalization with the absolute value of $\langle u'u'\rangle$, $\langle w'w'\rangle$ respectively $\langle u'w'\rangle$ as provided in the plot legend. As indicated in Fig. 4, the statistical uncertainty of all measured quantities follows an $a/\sqrt{N}$ law, indicating statistical independence of each sample and a normal distribution of the random error. The required number of samples to achieve 1% accuracy for mean velocities and, for example, 5% accuracy for variances and covariances strongly depends on the measurement position and the local turbulence intensity and spans two orders of magnitude. As a compromise, 10,000 samples are recorded per camera station with profile PIV, leading to uncertainties well below $1-2\%$ for U and W and below 6% for $\langle u'u'\rangle$ and $\langle w'w'\rangle$.

2.4 Consistency of turbulence statistics near the flat wall in comparison with DNS

Fig. 5 a), presents the mean axial velocity normalized by the friction velocity at two profile PIV measurement locations above the flat wall. In the viscous sublayer measurements coincide with $U^+ = z^+$ for both camera stations. Measured statistics are compared to DNS simulations of a channel flow between two

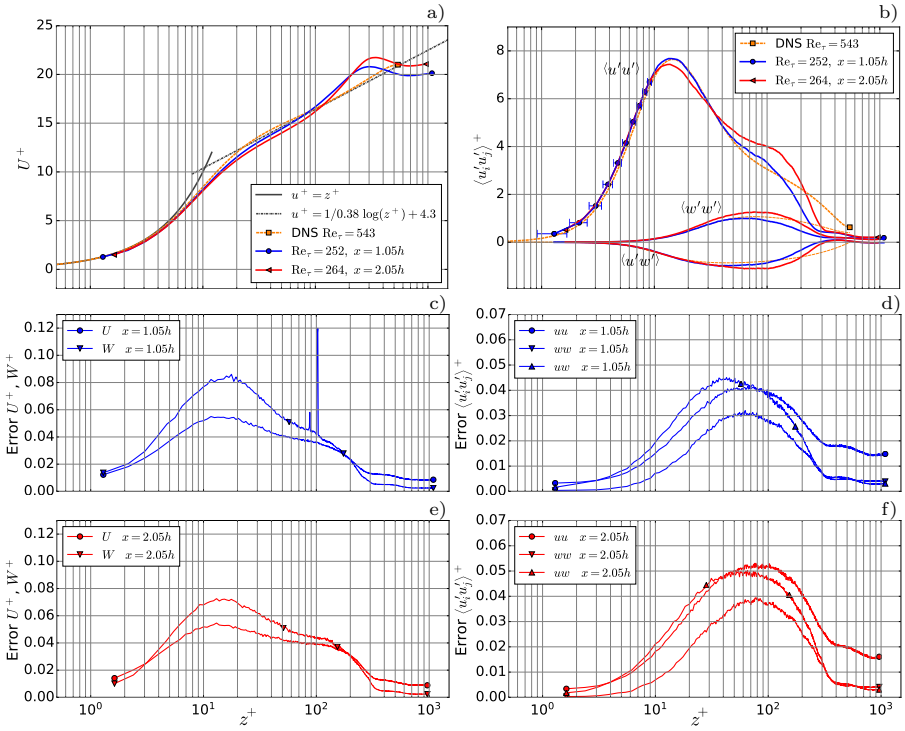

Fig. 5. Axial velocities above the flat wall (a) and Reynolds stress components (b) for ER 2.0 at $x = 1.05h$ and at $x = 2.05h$ and corresponding statistical uncertainties at $x = 1.05h$ (c, d) and at $2.05h$ (e, f).

parallel planes at $\mathrm{Re}_\tau = 543$ and $\mathrm{Re}_0 = 10,000$ by Lee and Moser [5] (the corresponding log-law is added to the plot). In the log-law region, U^+ approximately follows the DNS simulation. As indicated by the corresponding statistical uncertainties (c.f. Fig. 5 c, e), deviations in the log-law region and in the outer layer ($z+ > 100$) are likely to be attributed to the specific inlet flow of the tunnel or the adverse pressure gradient (APG). Distinct peaks near $z^+ = 100$ in the w-error distribution originate from pixel artifacts of the camera (c.f. Fig. 5 c).

Fig. 5 b), shows Reynolds stress components while statistical uncertainties are provided in subplots d) and f). Up to a wall distance of $z^+ = 10$, measurements at both stations have a slight bias with regard to DNS data which might be attributed to spatial resolution or spatial filtering by the PIV interrogation window. The bias along z^+ is in the order of 1 pixel, respectively below 0.43 wall units at $x = 1h$ and below 0.38 wall units at $x = 2h$. To visualize the size of one pixel for measurements at $x = 1h$, "error bars" corresponding to ± 1 pixel have been added to subplot b). With increasing wall distance up to $z^+ = 50$, $\langle u'u' \rangle$ and $\langle u'w' \rangle$ show a good agreement with the DNS data at $x = 1h$, while further downstream at $x = 2h$ strong influences of the adverse pressure gradient

are already noticeable, leading to a redistribution between Reynolds stress components (inner peak of $\langle u'u' \rangle$ decreases while $\langle u'w' \rangle$ increases). With increasing wall distance ($z^+ > 40$), the experimental data at $x = 1h$ shows a significant increase of the outer peak of $\langle u'u' \rangle$ in comparison to DNS data. This growth of the outer peak is much more pronounced further downstream at $x = 2h$ and is accompanied by an increase of magnitudes of $\langle w'w' \rangle$ and $\langle u'w' \rangle$.

3 Numerical method

Simulations were performed with DLR's solver for turbomachinery applications TRACE. TRACE solves the compressible Favre-averaged Navier-Stokes equations using a density-based, second order accurate, cell-centred finite volume method. Steady-state solutions are obtained with an implicit pseudo-time marching algorithm with local time stepping. Although the solver is not the natural choice for the simulation of an incompressible flow, it was applied because of the available turbulence models and the intended area of application. The differential Reynolds stress turbulence models (RSM) considered in this paper were Eisfeld's SSG/LRR-ω model [2] and a variant of Jakirlic's, Hanjalic's and Maduta's model [3] termed JH-ω^h, which are implemented in TRACE as described in [6]. RSMs were chosen because they are able to produce the turbulence induced secondary flows in rectangular duct geometries.

The domain of the diffuser was meshed in the interval $x/h \in [-3.15, 16]$ with $558 \times 90 \times 120$ cells ($6 \cdot 10^6$ in total). At the inlet, velocity profiles from the PIV measurements were extracted and prescribed in the solver as stagnation temperature, stagnation pressure and flow direction. The turbulent kinetic energy could also be approximated directly from the PIV data while the turbulent dissipation rate was chosen such that the turbulent decay on the centerline was matched. The outlet pressure was determined by a massflow controller to achieve conditions as measured in the wind tunnel. To increase the convergence rate of the compressible solver, conditions were scaled to an upstream Mach number of 0.1 while keeping the Reynolds number constant. It was ensured that this scaling had only a negligible effect on the normalised results. The mesh convergence as well as the scaling study are not described in this paper.

4 Mean flow field and comparison of turbulence models

An overview of the mean flow field at ER 2.0 is presented in Fig. 6 for the geometric symmetry plane of the diffuser at $y = 0$ (a, b) and for a plane near a side wall at $y/h = -0.46$ (c, d). As expected, the predominantly axial flow is decelerated over the diverging part of the wind tunnel (a). The PIV measurements show a backflow region between $x/h \approx 5$ and 7 at $y = 0$. Near the side wall, it starts at $x/h \approx 4$ and its vertical extent is reduced. The region of positive vertical velocity component W beginning between $x/h \approx 4$ and 5 on the symmetry plane (b) and the corresponding region of negative W near the side wall (d) indicate the presence of a corner vortex forming from the separated flow. On

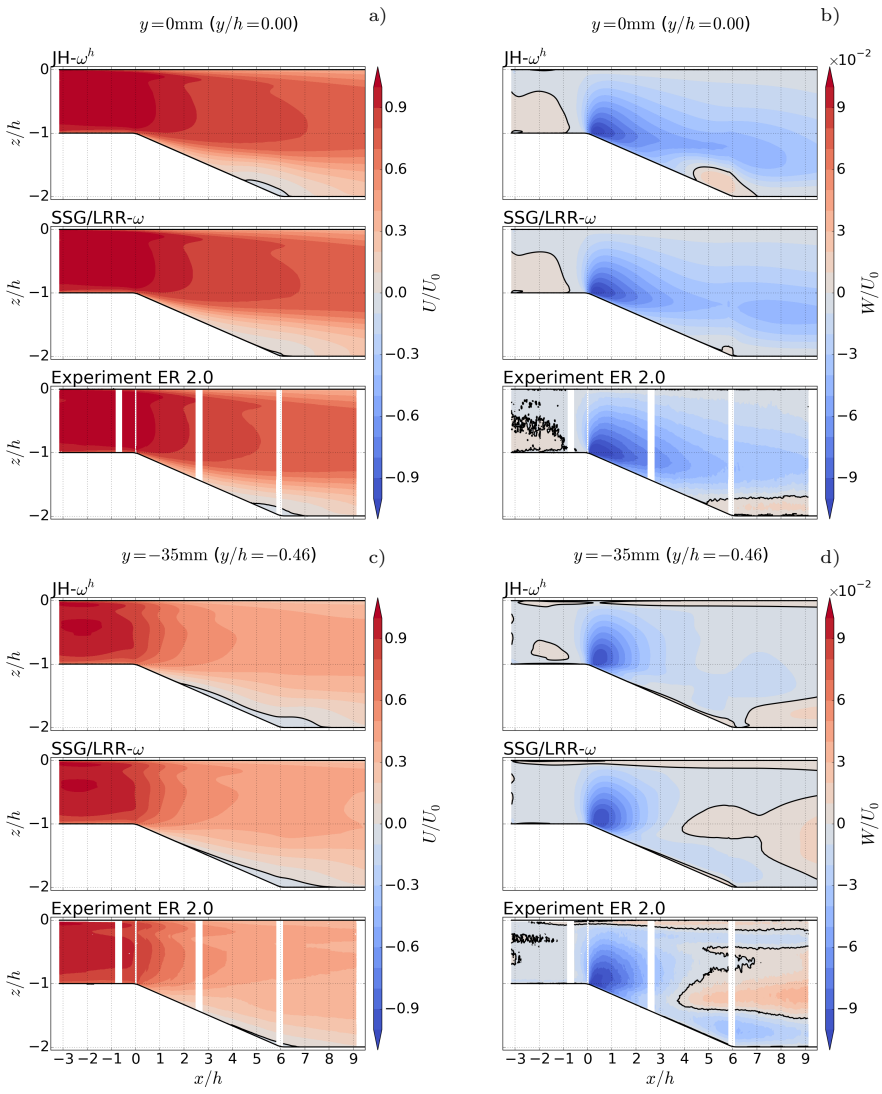

Fig. 6. Normalised axial U/U_0 (a, c) and vertical velocity component W/U_0 (b, d) at $y = 0$ (a, b) and $y/h = -0.46$ (c, d) computed with different turbulence models for ER 2.0 compared to PIV measurements. $U = 0$ is indicated as black contour line.

the top wall, one of the two corner vortices resulting from the rectangular shape of the duct, can be observed as area of positive W near the side wall (d). Its strength and shape is nearly independent of the choice of the APG. The third dominant feature hinting at a vortical structure is the large area of positive W filling the central region of the diffuser and downstream duct near the side wall (d).

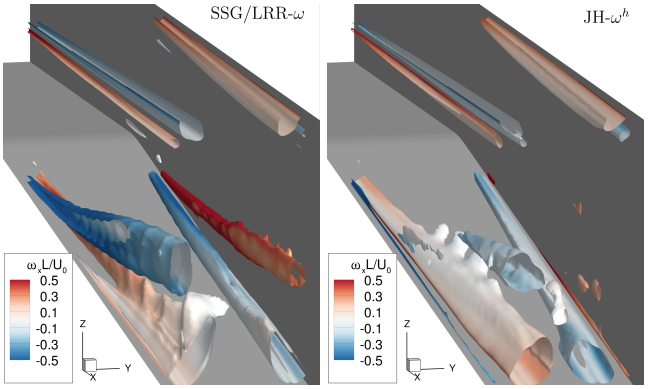

Fig. 7. Visualisation of vortices for different turbulence models between $x/h = 1$ and 5.3 using the Q-criterion. The isosurface at $Q = 10^4$ is coloured with the normalised axial vorticity $\omega_x L/U_0$.

The RSMs considered in this paper produce both quantitatively and qualitatively different flow fields compared with the experiment. This can best be seen in Fig. 7, which shows a closer view of the computed vortices in the diverging section of the wind tunnel using the Q-criterion for ER 2.0 only. Upstream of the diffuser and on the top wall, both RSMs show counter-rotating vortex pairs in each corner of the duct. Due to the non-symmetric inflow boundary condition, no symmetry about the plane $y = 0$ can be observed in the separating flow. Although both RSMs are able to produce the corner vortex pairs, they produce qualitatively different flow fields in and downstream of the diverging section. Looking at the $y < 0$ side of the diffuser, there is one vortex on the diverging wall with $\omega_x > 0$ (red) and one on the side wall with $\omega_x < 0$ (blue). In the solution computed with JH-ω^h, the blue vortex remains below the red vortex along the diverging section and downstream. In contrast, the blue vortex lifts from the diverging wall and follows a near horizontal trajectory along the side wall in the SSG/LRR-ω solution. Downstream, it dominates the secondary flow structure. The two models produce solutions which exhibit an opposing sense of rotation in the lower section of the wind tunnel. As described above, the measured vertical velocity near the side wall (see Fig. 6, d) shows a distinctly positive value. This is an indication towards a vortex system as predicted by the SSG/LRR-ω model.

Fig. 8 shows a quantitative comparison of the skin friction coefficient c_f with profile PIV measurements on the diverging wall. The extent of the backflow region ($c_f < 0$) agrees well with the area of $U < 0$ obtained with planar PIV. On the symmetry plane, both RSMs agree with the measurements concerning the separation point but show premature reattachment. Towards the side wall, both overestimate the extent and intensity of the backflow.

5 Conclusions and outlook

A generic experiment, consisting of a plane one-sided diffuser with variable expansion ratios, provides validation data for numerical simulations of corner separations and vortices in APGs. 2D-2C PIV was applied throughout the channel

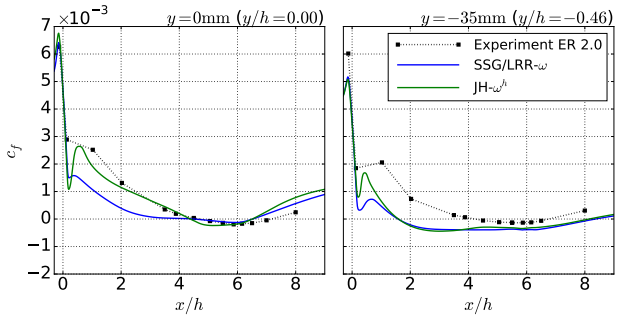

Fig. 8. Measured skin friction coefficient c_f on the diffuser wall in comparison to RANS results for $y = 0$ (centerline) and $y/h = -0.46$ at ER 2.0.

to provide boundary conditions and a global validation of mean velocities in the corner vortex flow. 1D-2C profile PIV was applied to evaluate the streamwise evolution of wall shear stress, to determine the skin friction coefficient and to provide turbulence statistics. Measurement uncertainties are estimated based on bootstrapping and depend on the local turbulence level. Consistency of near wall turbulence statistics is demonstrated by comparison with DNS. First RANS simulations of the full geometry using DLR's solver TRACE have revealed significant quantitative and qualitative differences between the different RSMs concerning the development of the vortex system over the corner separation. In future work, we will further evaluate the predictive quality of RSMs under the varying adverse pressure gradient using the turbulence statistics obtained from PIV.

References

1. Benedict, L.H., Gould, R.D.: Towards better uncertainty estimates for turbulence statistics. Experiments in Fluids **22**(2), 129–136 (1996)
2. Cécora, R.D., Radespiel, R., Eisfeld, B., Probst, A.: Differential Reynolds-stress modeling for aeronautics. AIAA J. pp. 1–17 (2014)
3. Jakirlić, S., Maduta, R.: Extending the bounds of steady RANS closures: Toward an instability-sensitive Reynolds stress model. Int. J. Heat Fluid Fl. **51**, 175 – 194 (2015). Theme special issue celebrating the 75th birthdays of Brian Launder and Kemo Hanjalic
4. Klinner, J., Willert, C.E.: Measurements of turbulent jet mixing in a turbulent coflow including the influence of periodic forcing and heating. Flow, Turbulence and Combustion **98**(3), 751–779 (2017)
5. Lee, M., Moser, R.D.: Direct numerical simulation of turbulent channel flow up to $Re_\tau \approx 5200$. Journal of Fluid Mechanics **774**, 395415 (2015)
6. Morsbach, C.: Reynolds stress modelling for turbomachinery flow applications. Dissertation, TU Darmstadt (2016)
7. Spalart, P.R.: Reflections on RANS modelling. In: S.H. Peng, P. Doerffer, W. Haase (eds.) Progress in Hybrid RANS-LES Modelling, *Notes on Numerical Fluid Mechanics and Multidisciplinary Design*, vol. 111, pp. 7–24. Springer Berlin / Heidelberg (2010)
8. Willert, C.E.: High-speed particle image velocimetry for the efficient measurement of turbulence statistics. Experiments in Fluids **56**(1), 17 (2015)